Received: 13 September 2021 | Revised: 17 February 2022 | Accepted: 26 February 2022

DOI: 10.1002/mop.33225

RESEARCH ARTICLE

WILEY

Near-high frequency antenna for unmanned aerial system ice-penetrating radar

Emily Arnold | **Ankur Patil** | **Fernando Rodriguez-Morales** | **Vincent Occhiogrosso**

Center for Remote Sensing of Ice Sheets, University of Kansas, Lawrence, Kansas, USA

Correspondence
Emily Arnold, Center for Remote Sensing of Ice Sheets, University of Kansas, Lawrence 66045, KS, USA.
Email: earnold@ku.edu

Funding information
National Science Foundation Office of Polar Programs, Grant/Award Number: OPP-1848210

Abstract

In this letter, we present the novel design of a near-high frequency antenna for a small unmanned aircraft systems helicopter for the intended purpose of sounding and imaging temperate glaciers. The antenna leverages concepts in the areas of efficient electrically small antennas, structural antennas, and impedance matching to create a versatile design that is small and lightweight yet robust for airborne operations and has wider bandwidth than existing designs.

KEYWORDS
airborne antennas, electrically small antenna, remote sensing

1 | INTRODUCTION

Airborne radars are effective tools in sounding polar ice,[1–4] yet critical regions (such as temperate mountain and outlet glaciers) tend to be the most difficult to sound[5–10] due to increased volume and surface scattering and the higher attenuation rate of warmer temperate ice. To reduce the effects of scattering and to improve clutter reduction, lower frequency radars are used (typically 2–60 MHz); however, the physically large antennas associated with these frequencies pose a significant technical problem for integration onto small unmanned aircraft systems (UAS). In light of the conclusions in ref. [11] as well as to balance frequency requirements and aircraft integration limitations, the Center for Remote Sensing of Ice Sheets developed two dual-frequency airborne sounders that operate around 14 MHz (Band 1 Mode) and 32 MHz (Band 2 Mode).[12,13] A high-power prototype flown from a Twin Otter and a miniaturized version flown from the 34 kg fixed-wing G1X UAS demonstrated improved penetration and ice-bottom detection compared to other ice sounders[12] when operating in the Band 2 Mode. Table 1 summarizes the Band 2 Mode parameters of the systems (known as the "High Frequency [HF] Sounder"). While the G1X system demonstrated promising capabilities, the deployment of this system has been limited due to the logistical complexities and costs associated with fixed-wing vehicles—namely, identifying areas suitable for runway construction and the need for highly skilled pilots and large field teams.

This letter presents a variant of the HF Sounder for AeroVironment's Vapor 55 helicopter UAS,[14] shown in Figure 1 with the antenna. The characteristics listed in the table in Figure 1 include the maximum payload mass for the vehicle as well as the mass of the antenna discussed in this study and the associated radar. The antenna mass listed in the table includes all associated support structures. While operational complexities are reduced for the helicopter, integration of a near-HF antenna on a platform lacking a long wingspan to support the antenna is more complicated. To our knowledge, the G1X design and the design presented in this study are the only instances of near-HF antennas installed on small UAS. While the general principles and methods related to electrically small antennas (ESAs), structural design, and impedance matching networks employed in our design procedure are well known, using

our multidisciplinary electro-mechanical approach we achieved a 30%–45% bandwidth improvement over the G1X design on a platform, that is, 25% smaller. This was achieved, in part, to a paradigm shift in design philosophies—namely, by moving away from low-profile antenna designs typically used for airborne antennas to a three-dimensional design, that is, load-bearing. The design presented is the first known carbon fiber reinforced plastic (CFRP) antenna installed in a relevant airborne platform environment and shown to have adequate structural and electrical properties.

2 | ANTENNA DESIGN

2.1 | Design goals

The design goals for the antenna were: (1) a center frequency between 30 and 40 MHz, (2) be electrically small and lightweight, (3) a 10-dB impedance bandwidth of ≥5 MHz, and (4) a gain of ≥−10 dBi across the operational bandwidth (with a peak gain close to 0 dBi). The size requirements were driven by the small UAS. The electrical requirements were based on the performance of other temperate ice sounders,[4,10] and the previous prototype HF Sounders, which provided sufficient vertical resolution and detection capabilities for the intended application. It is noted that low antenna gain is common among low-frequency airborne sounders, and it is a direct result of relatively low antenna radiation efficiency (RE) caused by integrating a large radiating structure onto a space-limited platform.

TABLE 1 HF sounder Band 2 parameter comparison

Parameter	Twin Otter[12]	G1X UAS[12]	This study
Center freq.	31.8 MHz	34.3 MHz	34.8/40.3 MHz
Bandwidth[a]	5.5 MHz	5 MHz	7.4/6.3 MHz
Trans. power	1000 W peak	100 W peak	100 W peak
Max antenna dim.	5 m	4 m	1.5 m

Abbreviations: HF, high frequency; UAS, unmanned aircraft systems.
[a]*Note*: ref. [12] reports the 8-dB bandwidth for the Twin Otter, which is 8 MHz.

2.2 | Efficient ESA concept

Given that a matching network would be required to achieve the desired impedance bandwidth, the initial focus was a small and efficient design. ESAs have low RE due to their small radiation resistance and large capacitive reactance, making them difficult to match to a 50 Ω source. Recently, Ziolkowski et al. published a series of "metamaterial-inspired" antenna designs that are both electrically small and have efficiencies near 100%.[15–19] Ziolkowski's Egyptian Axe Dipole (EAD) design[20] was identified as a candidate concept that could meet the physical limitations of the vehicle and be modified to serve as the landing gear. This planar design consists of a driven ESA dipole and a near-field resonant parasitic (NFRP) element with an inductor spanning the middle. The resonant frequency of the design is tuned by modifying the element geometry as well as the inductor. Figure 2 shows the initial EAD element tuned to resonate at 35.5 MHz ($ka = 0.55$) using Ansys's High Frequency Simulator Software (HFSS).[21] While the antenna RE was ~100%, the 10-dB bandwidth was only 1.8 MHz, well below the desired minimum of 5 MHz. In addition, this planar design does not have sufficient strength or stiffness to survive vehicle operations.

2.3 | Structural considerations

By replacing the original landing gear with a structural antenna, the vehicle payload limit is effectively increased by ~10%; however, the structure must be sized to withstand in-flight loads. Given the low speeds of the vehicle results in very low aerodynamic and inertial loads on the antenna, the dynamic response of the antenna thus drove the structural sizing. The vibrations created

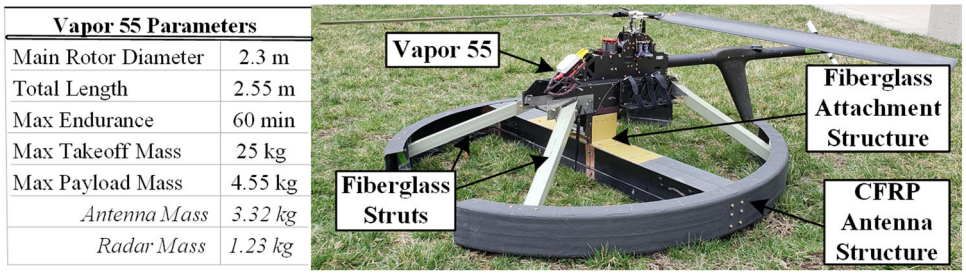

FIGURE 1 Vapor 55 helicopter with antenna

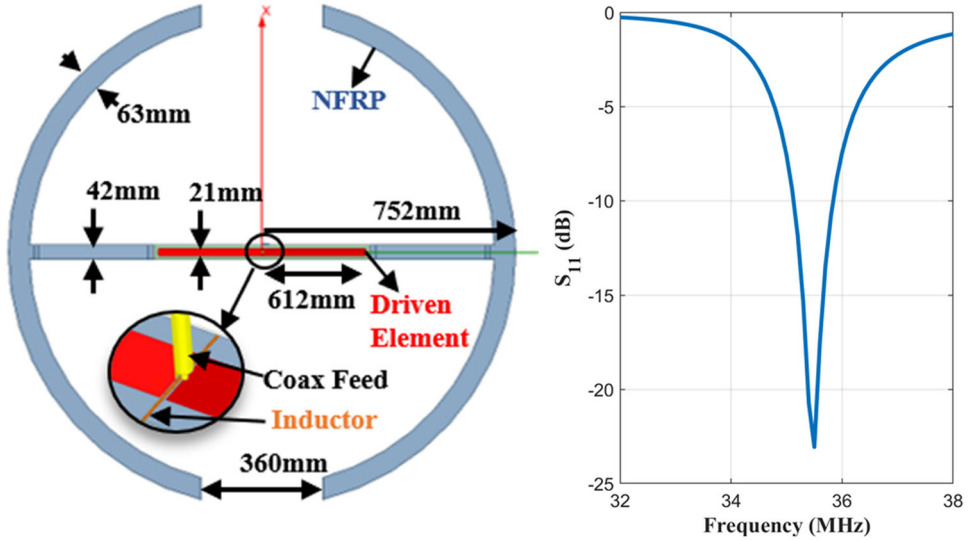

FIGURE 2 Preliminary EAD (left), and the simulated S_{11} (right). The inductor was modeled as a lumped component spanning a 0.79 mm gap. Both the driven and NFRP elements were modeled as copper and separated by a 0.76-mm thick substrate (dielectric constant of 2.2). EAD, Egyptian axe dipole; NFRP, near-field resonant parasitic

by the main rotor can excite potentially hazardous mechanical vibrations in the antenna resulting in structural failure or loss of vehicle control. In the design of large antenna structures mounted to air vehicles, the natural frequencies of the structure are tuned (by modifying the structure's stiffness and mass) to be outside the blade passage frequency of the propulsion system (s) by at least ±5 Hz.[22] For the three-bladed helicopter with a cruise revolution-per-minute (rpm) setting of 880, the antenna structure's natural frequencies must be 44 ± 5 Hz to avoid potentially dangerous dynamic responses.

To convert the EAD design shown in Figure 2 to a load-bearing component that could replace the original landing gear (hereafter referred to as the structural EAD or sEAD), the design variables considered were the material and section stiffness (i.e., the cross-section shape) The planar design was converted to a three-dimensional design and the antenna was fabricated from CFRP. Generally, the conductive elements of the antenna are made of metal with superior conductivity; however, the conductivity of CFRP is between 7000 and 13 000 S/m at VHF frequencies, and in Patil and Arnold,[23] it was shown that antennas fabricated with CFRP biaxial cloth material resonated at the same frequency and had radiation efficiencies within 10% of identical copper antennas. Due to lower specific strength and stiffness, equivalent sections of copper or aluminum would be 50%–500% heavier than CFRP sections; given the severe payload limitations of the UAS, a metallic antenna design would not meet the weight restrictions. Thus, the first step to ensuring a lightweight structural antenna was to use CFRP for the NFRP element.

Next, to improve the section stiffness, the area moment of inertia (MOI)—a geometric property of a cross-section that indicates a beam's ability to resist bending—must increase. For a rectangular beam, the relationship between a section's MOI, width, w, and height, h, is

$$MOI = \frac{1}{12} w h^3. \tag{1}$$

From Equation (1), it is clear that increasing the height of a section has the largest influence on increasing the MOI, and that the planar antenna in Figure 2 would have a near-zero MOI.

Through a series of parametric analyses in HFSS, the design in Figure 2 was converted to the robust design shown in Figures 1 and 3. While the design maintains the radius of the planar design, the center section of the NFRP has an "I" cross-section, and the arms have a "C" cross-section to improve the antenna stiffness (MOIs of ~407 cm^4 for both). The height of the NFRP is 127 mm, and the cap widths (horizontal portion of the sections) of the center section and arcs are 133 and 65 mm, respectively. The cross-section size and shape were chosen to achieve optimized electrical performance based on the results from ref. [24]. The NFRP was fabricated using AS4 3k biaxial plain weave (0°/90°) fabric with epoxy resin (DPL 40) and a wet-layup technique. The arcs are composed of three layers of CRFP and center I-beam is composed of four layers of CFRP. The arcs and I-beam were mechanically joined using custom aluminum brackets. Given

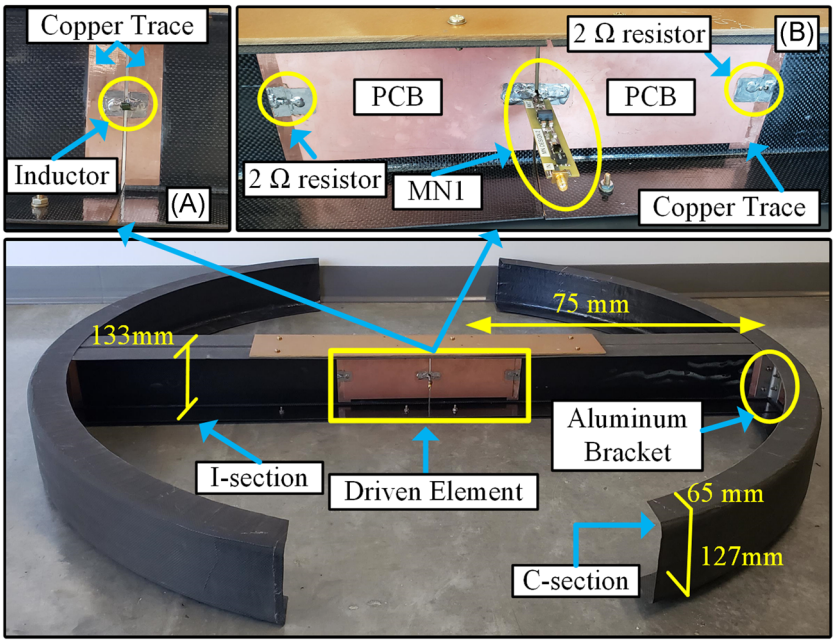

FIGURE 3 The bottom image shows the fabricated structural EAD prototype. The center section of the NFRP element has an I cross-section while the arms have C cross-section. Inset (A) shows the backside of the center section highlighted by the yellow box. The 110-nH inductor can be seen spanning a 2-mm gap between the two NFRP arms with copper traces cocured in the laminate to facilitate soldering the component. Inset (B) shows the front side of the center section. The balanced MN1 design is connected to the two arms of the driven element and resistors are soldered on either side to an embedded copper trace in the NFRP laminate. EAD, Egyptian axe dipole; NFRP, near-field resonant parasitic

that the resin is an insulator and the difficulty in soldering to CFRP, thin copper traces were embedded in the laminate where soldering and electrical connections were required. An air-core 110-nH lumped inductor (Coilcraft) was soldered to the copper on the backside of the NFRP to tune the resonant frequency (Figure 3A). The driven element (dimensions of $102 \times 175 \times 1.57\ \text{mm}^3$) is oriented vertically on the web of the center section and was fabricated from a 1.57-mm thick FR4 printed circuit board (PCB). The initial prototype was fed via a coax cable soldered to either arm of the driven element. Finally, the long unsupported arms of the arc required additional struts to ensure the antenna's natural frequency was ±5 Hz outside the blade passage frequency of 44 Hz. As seen in Figure 1, four $44.5\ \text{mm}^2$ fiberglass tubes connect the arcs to the vehicle body. A modal test was performed on the prototype and the two closest frequencies to the blade passage frequency were found to be at 31.2 and 88.1 Hz, thus satisfying the structural requirements.[25]

2.4 | Impedance matching for improved bandwidth

Given the relatively low gain requirement, bandwidth was prioritized. The antenna's near-zero resistance in the 30–35 MHz band makes matching difficult, so a 0402 2 Ω surface-mount resistor was added across each arm of the driven and NFRP elements for resistive loading of the initial prototype (see Figure 3B, total of two resistors added). The use of resistors and CFRP materials reduced the antenna RE to ~80%. Resistors with a larger footprint will be used for the final version of the antenna to sustain the required 5 W average power produced by the radar transmitter (100 W peak with 5% duty cycle). However, this change will not alter the performance or physical dimensions of the antenna.

To further improve the sEAD bandwidth in the 30–40 MHz range and add versatility to the antenna, two matching networks (MNs) were synthesized using Genesys (Keysight Technologies©, ver 2015.08). The first MN design (MN1) prioritized maximizing bandwidth across a lower frequency band using a fifth order LC impedance MN. The second MN design (MN2) prioritized gain and was designed around the antenna's natural center frequency of 40.4 MHz using a third order topology. Using a technique similar to that described in ref. [26], the LC networks were converted into balanced configurations followed by a 1:1 balun. In both cases, the balun is a commercially off-the-shelf wideband 1:1 RF transformer in surface mount package (Coilcraft PWB1010-1L), and it has a measured insertion loss of

<0.5 dB over the 30–45 MHz range. The common-mode rejection ratio computed from its measured S-parameters is 30–34 dB (over the same frequency range). As with the surface-mount resistors discussed above, an equivalent wire-wound transformer with ferrite core will replace the balun used in the initial prototypes. This will increase the power handling of the antenna to at least 5 W average without impacting size or weight of the matching network in a significant manner. The designs were EM/circuit co-simulated and optimized using Advanced Design System (ADS; Keysight Technologies©, ver 2016.01) with the measured antenna impedance as the circuit load. Figure 4 provides a schematic for both MN designs, and Figure 3B shows the fabricated MN1 attached to the antenna.

3 | SIMULATION AND MEASUREMENT RESULTS

Figure 5 is the normalized radiation pattern of the antenna without matching network at 40 MHz. As expected, the pattern is that of a standard dipole. Figure 6 compares the sEAD simulated and measured scattering parameters (S_{11}) both with and without the MNs. The 1 MHz downward shift in the center frequency between the measured and simulated results of the sEAD without MN is attributed to the coax feed (effectively increasing the electrical length) not included in the simulations. The sEAD 10-dB bandwidth increased to 7.3 and 6.4 MHz with MN1 and MN2, respectively. Overall, the simulated and measured MN results agreed well; however, the 0.5–0.8 MHz bandwidth reduction in the measured MN results is attributed to typical variations in capacitor values (±5%). This was verified via a sensitivity analysis in ADS. Figure 6 also includes the S_{11} when installed on the vehicle. Despite the MNs being tuned without the vehicle, the installed response varied minimally—indicating the vehicle's presence has very little effect on the antenna input impedance.

Figure 7 compares the simulated and measured gain of the antenna for different test cases. The gain measurements were conducted using the gain-transfer method and an ETS 3142C antenna as the reference antenna. The simulated and measured gains of the sEAD without MN agreed well, and the peak gains occurred at the resonant frequencies. For the MN1 design, the maximum gain shifted to 38 MHz and was ~1.5 dB down from the maximum gain without MN, which is approximately the two-way loss of MN1. However, the gain was improved by an average of 3 dB over the bandwidth while also achieving lower S_{11} with respect to the unmatched case. For MN2, the gain varied from a peak of −0.5 to −2 dBi across its bandwidth—a significant increase over the MN1

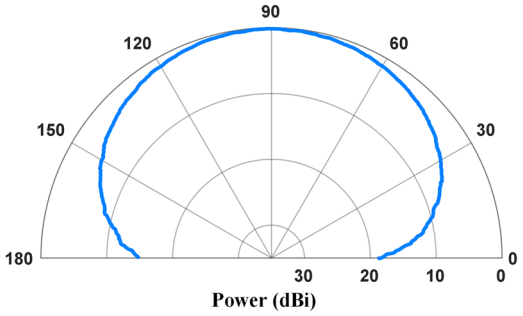

FIGURE 5 Normalized radiation pattern of the antenna without MN. MN, matching network

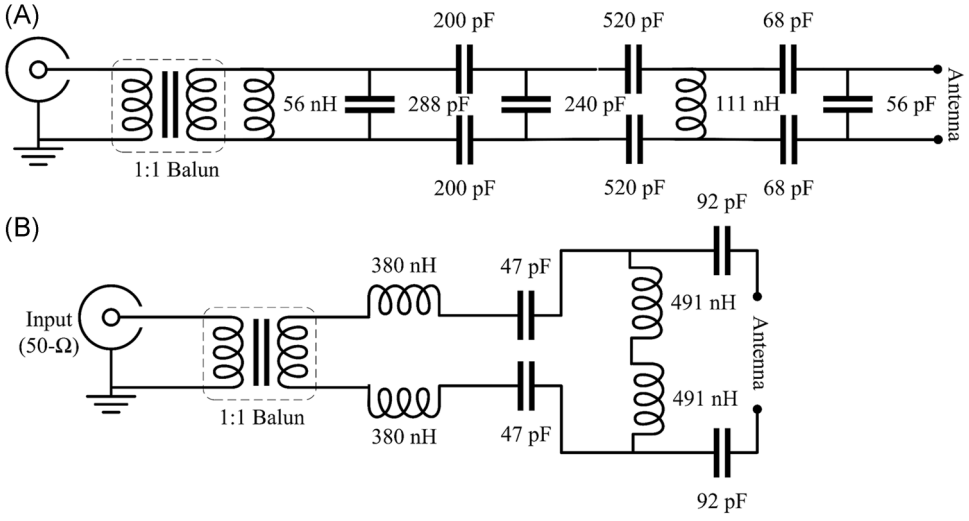

FIGURE 4 Inset (A) MN1 and inset (B) MN2 with nominal component values. MN, matching network

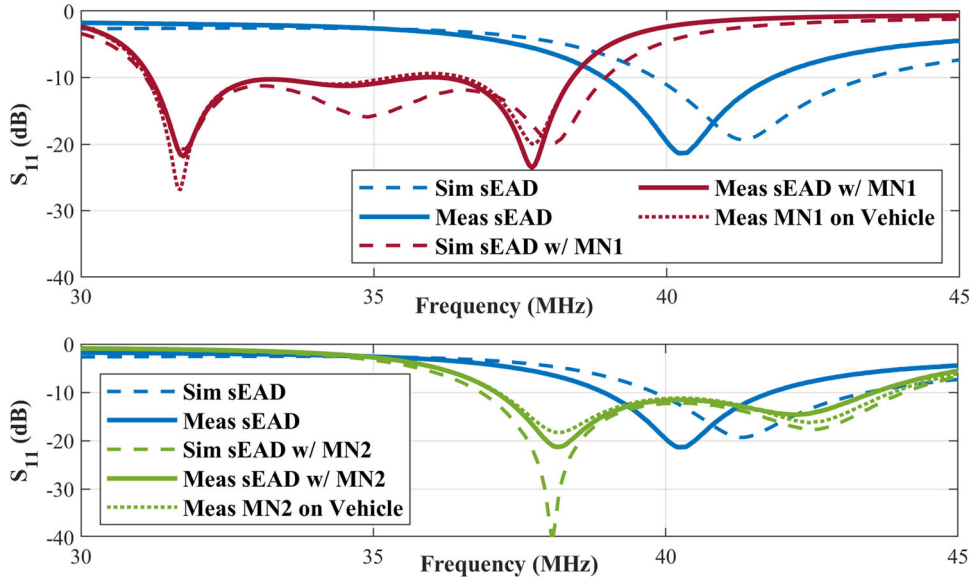

FIGURE 6 Simulated and measured sEAD with and without MNs (top: MN1, bottom: MN2). MN, matching network; sEAD, structural Egyptian axe dipole

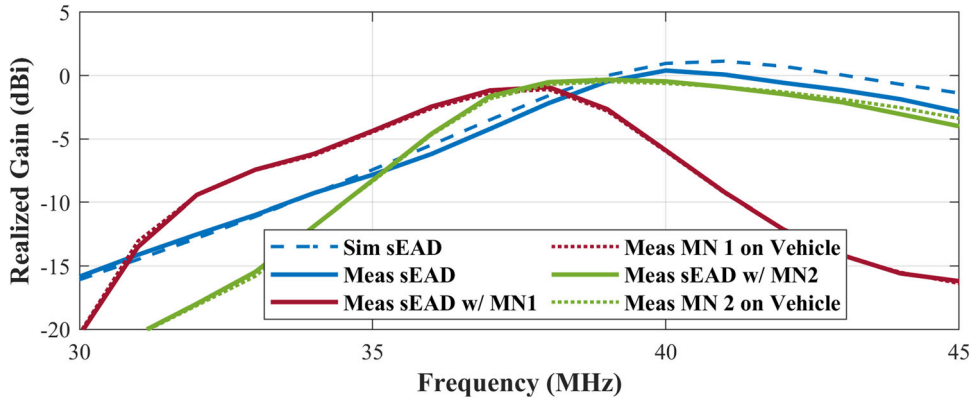

FIGURE 7 sEAD gain for various configurations. sEAD, structural Egyptian axe dipole

gain. Again, a 1 dB decrease in peak gain is attributed to the inclusion of the MN.

4 | CONCLUSIONS

Using a multidisciplinary electro-mechanical approach that leveraged techniques in efficient ESAs, structural antennas, and impedance matching, we developed a versatile near-HF antenna for a small UAS. While further refinement of the MNs is planned, the two initial designs provide flexible performance characteristics—namely, the option between lower frequency or higher gain. The performance of our innovative design has improved bandwidth over previous HF Sounder prototypes, but with a significantly smaller profile. We expect to deploy the system to Greenland in 2022.

ACKNOWLEDGMENT

This study was supported by National Science Foundation Office of Polar Programs, OPP-1848210.

DATA AVAILABILITY STATEMENT

The data that support the findings of this study are available from the corresponding author upon reasonable request.

ORCID

Emily Arnold http://orcid.org/0000-0002-4427-6362
Ankur Patil http://orcid.org/0000-0002-4114-7012

Fernando Rodriguez-Morales http://orcid.org/0000-0001-8004-6145
Vincent Occhiogrosso http://orcid.org/0000-0003-2125-4491

REFERENCES

1. Waite H, Schmidt SJ. Gross errors in height indication from pulsed radar altimeters operating over thick ice or snow. *Proc IRE*. 1961;(5):38-53.
2. Gogineni S, Chuah TS, Allen C, Jezek K, Moore RK. An improved coherent radar depth sounder. *J Glaciol*. 1998; 44(148):659-669. doi:10.3189/S0022143000002161
3. Peters M, Blankenship DD, Carter SP, Kempf SD, Young DA, Holt JW. Along-track focusing of airborne radar sounding data from West Antarctica for improving basal reflection analysis and layer detection. *IEEE Trans Geosci Remote Sens*. 2007; 45(9):2725-2736. doi:10.1109/TGRS.2007.897416
4. Rignot E, Mouginot J, Larsen CF, Gim Y, Kirchner D. Low-frequency radar sounding of temperate ice masses in Southern Alaska. *Geophys Res Lett*. 2013;40(20):5399-5405.
5. Griggs JA, Bamber JL. Antarctic ice-shelf thickness from satellite radar altimetry. *J Glaciol*. 2011;57(203):485-498. doi:10.3189/002214311796905659
6. Bamber JL, Gomez-Dans JL, Griggs JA. A new 1 km digital elevation model of the Antarctic derived from combined satellite radar and laser data – part 1: data and methods. *Cryosphere*. 2009;3(1):101-111. doi:10.5194/tc-3-101-2009
7. Fountain AG, Jacobel RW, Schlichting R, Jansson P. Fractures as the main pathways of water flow in temperate glaciers. *Nature*. 2005;(433):618-621.
8. Herreid S, Pellicciotti F. The state of rock debris covering Earth's glaciers. *Nat Geosci*. 2020;13:621-627.
9. MacGregor JA, Li J, Paden J, et al. Radar attenuation and temperature within the Greenland Ice Sheet. *J Geophys Res: Earth Surf*. 2015;121(120):983-1008. doi:10.1002/2014JF003418
10. Conway H, Smith B, Vaswani P, Matsuoka K, Rignot E, Claus P. A low-frequency ice-penetrating radar system adapted for use from an airplane: test results from Bering and Malaspina Glaciers, Alaska, USA. *Ann Glaciol*. 2009; 50(51):93-97. doi:10.3189/172756409789097487
11. MacGregor JA, Studinger M, Arnold E, Leuschen CJ, Rodriguez-Morales F. Brief communication: an empirical relation between center frequency and measured thickness for radar sounding of temperate glaciers. *Cryosphere*. 2021;15:2569-2574.
12. Arnold EJ, Rodriguez-Morales F, Paden J, et al. HF/VHF radar sounding of ice from manned and unmanned airborne platforms. *Geosciences*. 2018;8(5):182.
13. Arnold EJ, Leuschen C, Rodriguez-Morales F, Li J, Hale R, Keshmiri S. CReSIS airborne radars and platforms for ice and snow sounding. *Ann Glaciol*. 2019;(81):1-10. doi:10.1017/aog.2019.37
14. AeroVironment Vapor Website. https://www.avinc.com/uas/vapor
15. Ziolkowski RW, Jin P, Lin C-C. Metamaterial-inspired engineering of antennas. *Proc IEEE*. 2011;99(10):1720-1730.
16. Erentok A, Ziolkowski RW. Metamaterial-inspired efficient electrically small antennas. *IEEE Trans Antennas Propag*. 2008;56(3):691-707.
17. Ziolkowski RW, Kipple A. Application of double negative metamaterials to increase the power radiated by electrically small antennas. *IEEE Trans Antennas Propag*. 2003;15: 2626-2640.
18. Ziolkowski RW, Kipple A. Reciprocity between the effects of resonant scattering and enhanced radiated power by electrically small antennas in the presence of nested metamaterial shells. *Phys Rev E*. 2005;72(036602).
19. Erentok A, Ziolkowski RW. A hybrid optimization method to analyze metamaterial-based electrically small antennas. *IEEE Trans Antennas Propag*. 2007;55:731-741.
20. Ziolkowski RW. Low profile, broadside radiating, electrically small Huygens source antennas. *IEEE Access*. 2015;3: 2644-2650.
21. Ansys® Electromagnetics Suite, ver. 2019.
22. Hale R, Arnold E, Ewing M, Lui W. Method for design and analysis of externally mounted antenna fairings in support of cryospheric surveying. Paper presented at: AIAA Structures, Structural Dynamics and Materials Conference; April 2011; Denver, CO.
23. Patil A, Arnold E. Characterizing carbon fiber composite conductivity for VHF structural antenna applications. *IEEE Trans Antennas Propag*. 2021;13:549-556. doi:10.1109/TAP.2021.3102037
24. Patil AS, Arnold E. Characterization of standard structural CFRP beam shapes for UAS VHF antenna applications. Paper presented at: AIAA SciTech Conference Proceeding. 2021:1803.
25. Burns J, Arnold E, Ballingu U. Weight-optimized structural antenna concept for UAS remote sensing. Paper presented at: AIAA SciTech Forum and Exposition; 2022; San Diego, CA.
26. Hawkins J, Lok LB, Brennan PV, Nicholls KW. HF wire-mesh dipole antennas for broadband ice-penetrating radar. *IEEE Antennas Wirel Propag Lett*. 2020;19(12):2172-2176.

How to cite this article: Arnold E, Patil A, Rodriguez-Morales F, Occhiogrosso V. Near-high frequency antenna for unmanned aerial system ice-penetrating radar. *Microw Opt Technol Lett*. 2022;1-7. doi:10.1002/mop.33225